Biomechanics and Modeling in Mechanobiology (2018) 17:727–743
https://doi.org/10.1007/s10237-017-0989-0

ORIGINAL PAPER

Modeling mechanical inhomogeneities in small populations of proliferating monolayers and spheroids

Emma Lejeune[1] · **Christian Linder**[1]

Received: 22 September 2017 / Accepted: 16 November 2017 / Published online: 2 December 2017
© Springer-Verlag GmbH Germany, part of Springer Nature 2017

Abstract
Understanding the mechanical behavior of multicellular monolayers and spheroids is fundamental to tissue culture, organism development, and the early stages of tumor growth. Proliferating cells in monolayers and spheroids experience mechanical forces as they grow and divide and local inhomogeneities in the mechanical microenvironment can cause individual cells within the multicellular system to grow and divide at different rates. This differential growth, combined with cell division and reorganization, leads to residual stress. Multiple different modeling approaches have been taken to understand and predict the residual stresses that arise in growing multicellular systems, particularly tumor spheroids. Here, we show that by using a mechanically robust agent-based model constructed with the peridynamic framework, we gain a better understanding of residual stresses in multicellular systems as they grow from a single cell. In particular, we focus on small populations of cells (1–100 s) where population behavior is highly stochastic and prior investigation has been limited. We compare the average strain energy density of cells in monolayers and spheroids using different growth and division rules and find that, on average, cells in spheroids have a higher strain energy density than cells in monolayers. We also find that cells in the interior of a growing spheroid are, on average, in compression. Finally, we demonstrate the importance of accounting for stochastic fluctuations in the mechanical environment, particularly when the cellular response to mechanical cues is nonlinear. The results presented here serve as a starting point for both further investigation with agent-based models, and for the incorporation of major findings from agent-based models into continuum scale models when explicit representation of individual cells is not computationally feasible.

Keywords Peridynamics · Tumor growth · Morphogenesis · Cell division

Mathematics Subject Classification 92C10 · 74L15

1 Introduction

As a population of cells grows and divides, cells both experience and generate mechanical forces. And, as an entire population arises from an initial single cell, the local heterogeneity of the emerging chemical and mechanical microenvironment leads to spatially dependent cell behavior (Sutherland 1988). For example, as the size of a tumor spheroid increases, cells located near the center of the spheroid have limited access to nutrients compared to cells closer to the spheroid edge and are more likely to become either quiescent or necrotic (Kim et al. 2007). In addition to the chemical microenvironment, the mechanical microenvironment is important because elevated levels of compressive stress will decrease cell growth and proliferation rates, and alter cell death rates (Galle et al. 2009). As illustrated in Fig. 1, an avascular spheroidal cell population may develop a layered structure with a necrotic core, a quiescent internal region, and a proliferating rim (Folkman and Hochberg 1973). In the context of tumor growth, stress-suppressed growth may limit a tumor's ability to expand and infiltrate surrounding tissue (Roose et al. 2003; Byrne and Preziosi 2003; Helmlinger et al. 1997). However, many cancer drug therapies specifically target rapidly proliferating cells, so slowed rates of cell proliferation due to mechanical compression may render drug therapies less effective (Mascheroni et al. 2017). Furthermore, certain cells

✉ Christian Linder
linder@stanford.edu

Emma Lejeune
elejeune@stanford.edu

[1] Department of Civil and Environmental Engineering, Stanford University, Stanford, CA 94305, USA

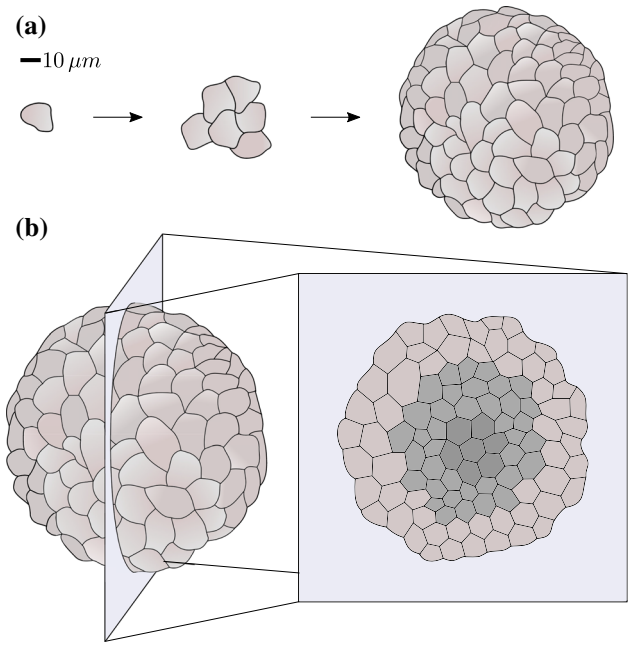

Fig. 1 **a** Avascular tumor spheroid growth driven by cell proliferation starting from a single cell; **b** As an avascular tumor spheroid grows, it develops a layered structure with a necrotic core, a quiescent internal region, and a proliferating rim (Folkman and Hochberg 1973). This layered structure arises due to local differences in the chemical and mechanical microenvironment within the growing spheroid (Sutherland 1988). Subsequent changes in cell biological function across layers often intensify differences in local conditions.

may respond to a hostile microenvironment by switching to a more aggressive phenotype (Janet et al. 2012). As a tumor undergoes angiogenesis, a robust understanding of the local mechanical environment is critical for developing effective treatment strategies (Stylianopoulos 2017; Vavourakis et al. 2017; Stylianopoulos et al. 2013; Mpekris et al. 2015). A mechanistic understanding of the residual stresses generated as a cell population develops from a single cell is fundamental to investigating the relationship between the microenvironment and these critical outcomes. And, given that many in vitro experiments relevant to developing new cancer treatment are conducted in a two-dimensional setting, there is utility in investigating and comparing both the two-dimensional (monolayer) and three-dimensional (spheroid) cases (Breslin and O'Driscoll 2013). In this paper, we take a simulation based approach to understanding the residual stresses and stochastic fluctuations in residual stresses that emerge from cell growth and division in small populations of multicellular monolayers and spheroids.

Due to the complexity of biological systems, predicting the residual stresses within a proliferating population of cells is not trivial. Even in examining the simple case of a freely growing radially symmetric tumor spheroid, different model assumptions lead to quantitatively and qualitatively different results. In Table 1, we show a few representative examples from the literature on computational modeling of freely growing avascular tumor spheroids. Some models predict that the interior of a freely growing tumor spheroid is in tension, while others predict that it is in compression.

Probing the residual stress state in avascular tumor spheroids has also been approached in the experimental setting, and computational models have been developed in order to interpret experimental observations. For example, by extracting and cutting a murine tumor spheroid (an example of a spheroid growing under mechanical confinement) and comparing it to a finite element simulation, researchers were able to determine that the center of the tumor was in compression because it expanded when released by the cut (Stylianopoulos et al. 2012). The discrepancy between different model predictions shown in Table 1 emphasizes

Table 1 Selected examples from the literature on computational modeling of freely growing avascular tumor spheroids. Studies are listed in chronological order. Notably, some models predict tension in the spheroid center while others predict compression

References	Model description	Stress state at the spheroid center
Jones et al. (2000)	Linear elastic constitutive law with a growth term that is related to nutrient concentrations	Tension
Ambrosi and Mollica (2002)	Continuum mechanics with volumetric growth, growth term is a function of spheroid radius	Tension
Araujo and McElwain (2004)	Extension of Jones et al. (2000) to include an anisotropic growth law that depends on both nutrient concentrations and stress state	Tension
Drasdo and Höhme (2005)	Individual cell based model with explicit cell division, cell growth depends on nutrient concentration and stress state	Compression
Xue et al. (2016)	Poroelastic theory, anisotropic growth, growth is related to nutrient concentration and stress state	Tension
Ambrosi et al. (2016)	Poroelastic theory, growth is related to nutrient concentration and stress state	Compression

that numerical models require experimental validation before broader implementation. However, with smaller populations of cells, such as in three-dimensional in vitro cell culture, experimentally probing the mechanical state is comparatively difficult. This difficulty stems from both technological limitations, in that attempting to "cut" tissue on the microscale without generating confounding multiphysics effects is very challenging, and the fact that behavior at the cellular scale is highly stochastic thus requiring a high number of experiments to build a complete picture. Despite present limitations, quantifying residual stresses in cell populations is a highly active area of research, and significant advances are anticipated in the near future (Sugimura et al. 2016).

In this paper, we use a recently developed mechanically robust agent-based model to understand how residual stresses emerge from cellular scale growth and division, and report and discuss the stochastic fluctuations in residual stress within proliferating monolayers (two-dimensional) and spheroids (three-dimensional). Unlike previous agent-based studies of monolayers and spheroids which focused on cell populations of thousands of cells (Drasdo and Höhme 2005), we focus on small cell populations (1–100 s of cells) and instead run thousands of stochastic simulations to paint a clear picture of system behavior. In this initial study, we focus exclusively on mechanically regulated growth rather than growth regulated by nutrient availability. Nutrient transport plays a significant role in the development of larger multicellular systems (Preziosi and Tosin 2008); however, in smaller spheroids and monolayers with a constant nutrient supply, the contribution of nutrient transport is less significant and position dependent growth suppression can arise through considering the effects of the mechanical microenvironment alone (Drasdo and Höhme 2005; Galle et al. 2009). In this initial study, we do not investigate the effects of confining pressure from a surrounding material. Confining pressure plays a significant role in vivo and has been explored in several recent in vitro studies (Cheng et al. 2009), but we limit the scope of this paper to the starting point of freely growing monolayers and spheroids.

Within this scope, we explore multiple different algorithmic rules for cell growth and cell division orientation, including the "long axis rule" for cell division. The "long-axis rule" states that when cells divide the division plane is perpendicular to their longest axis. In our model, the longest axis is determined based on local stress state. Because mechanisms such as cell division are modeled explicitly in an agent-based model, it is meaningful to implement them on the cellular scale and subsequently observe how their influence emerges on the population scale. Furthermore, we report stochastic fluctuations in the isochoric stress of cells within the population and investigate an example of a stress-dependent growth rule where accounting for the stochastic fluctuations is critical. Insights from this agent-based modeling approach add to the fundamental understanding of monolayer and spheroid growth and will help inform future continuum models derived from behavior on the cellular scale (Byrne and Drasdo 2008) where accounting for stochastic behavior is critical (Lima et al. 2015). Specifically, agent-based models may be used to delineate the contributions of elastic-, plastic-, and growth-induced mechanical response in continuum models (Ambrosi and Preziosi 2008), or the agent-based models themselves can be incorporated into a multiscale framework (Rahman et al. 2017).

The remainder of this paper is organized as follows. In Sect. 2, we introduce the model used to investigate the mechanical state of a growing cell population. In Sect. 2.1, we detail the basics of peridynamics, the method used to maintain mechanical equilibrium, and in Sects. 2.2, 2.3, and 2.4, we describe the algorithmic rules used to control cell growth, cell division, and the dimension of population morphology. We present the results of our simulations in Sect. 3. In Sect. 3.1, we compare different algorithmic growth and division laws by examining the average strain energy density per cell. Then, in Sect. 3.2, we look at the spatial distribution of isochoric stress in a population of growing cells. In Sect. 3.3, we show the outcomes of implementing a growth law where isochoric stress suppresses cell growth. We conclude in Sect. 4.

2 Mechanical model

Computational modeling is a powerful tool for investigating multicellular systems (Taber 1995). Computational models are used to interpret in vitro experimental results (Jagiella et al. 2016), understand coupling between specific mechanisms guiding cell population and tissue behavior (Ambrosi and Pezzuto 2012; Tepole and Kuhl 2016), connect observations in the in vitro setting to practical applications in vivo (Lorenzo et al. 2016; Deisboeck et al. 2011), and elucidate mechanically driven global system responses such as geometric instability (Lejeune et al. 2016; Drasdo and Loeffler 2001; Dortdivanlioglu et al. 2017; Giverso and Ciarletta 2016). In this paper, we focus on capturing the heterogeneous mechanical microenvironment of cellular monolayers and spheroids. Because we are interested in modeling small populations of 1–100s of cells, we approach this problem with an agent-based computational model that treats each cell as a discrete entity. Agent-based models are particularly well suited for this application because they capture emergent behavior where rules applied on the cellular scale manifest on the population scale (Drasdo et al. 2007; Galle et al. 2006; Wang et al. 2015). In Sect. 2.1, we introduce the mechanical foundation of our model. Then, in Sect. 2.2, we describe the algorithm used to prescribe growth of an individual cell, in Sect. 2.3 we present the "long axis rule" governing

the orientation of cell division, and in Sect. 2.4, we explain the difference between out two-dimensional monolayer and three-dimensional spheroid implementations.

2.1 Peridynamic agent-based cell model

The purely mechanical components of our model are based on peridynamics, a theoretical and computational framework initially proposed as an alternative to classical continuum mechanics with fracture problems in mind (Silling 2000). Here, we very briefly describe the discrete form of the peridynamic equation of motion. Additional details, particularly toward implementing our chosen linear elastic constitutive law with a growth term, are given in Appendix A and our previous publication (Lejeune and Linder 2017a).

With peridynamics, the equation of motion at node j is formulated as a summation that includes the interactions between j and all points k within a defined interaction distance. To formulate the peridynamic equation of motion, we start by defining the horizon $\mathcal{H}_\mathrm{j}$ of a node. The size of the horizon is defined by an interaction distance δ_j, written as

$$\delta_\mathrm{j} = 2(1 + g_\mathrm{j}) r_0 \, \delta_\mathrm{j}^0 \tag{1}$$

where g_j is the radial growth of node j, r_0 is the baseline radius of node j, and δ_j^0 is a prescribed value meant to ensure that immediate neighbors of node j will be within $\mathcal{H}_\mathrm{j}$. The horizon $\mathcal{H}_\mathrm{j}$, illustrated in Fig. 2, is then defined as

$$\mathcal{H}_\mathrm{j} = \{\mathrm{k} \mid \; ||\boldsymbol{y}_\mathrm{k} - \boldsymbol{y}_\mathrm{j}|| < \delta_\mathrm{j}\} \tag{2}$$

where $\boldsymbol{y}_\mathrm{j}$ and $\boldsymbol{y}_\mathrm{k}$ are nodal positions in the current configuration. We subsequently define the dual horizon of node j as

$$\mathcal{H}'_\mathrm{j} = \{\mathrm{k} \mid \; \mathrm{j} \in \mathcal{H}_\mathrm{k}\}\,. \tag{3}$$

With $\mathcal{H}_\mathrm{j}$ and $\mathcal{H}'_\mathrm{j}$ defined, we write the dual-horizon peridynamics equation of motion at static equilibrium in the absence of body forces as

$$0 = \sum_{\mathrm{k}\in\mathcal{H}'_\mathrm{j}} \boldsymbol{f}_\mathrm{jk}(\boldsymbol{y}_\mathrm{j}, \boldsymbol{y}_\mathrm{k})\, \Delta V_\mathrm{k} - \sum_{\mathrm{k}\in\mathcal{H}_\mathrm{j}} \boldsymbol{f}_\mathrm{kj}(\boldsymbol{y}_\mathrm{j}, \boldsymbol{y}_\mathrm{k})\, \Delta V_\mathrm{k} \tag{4}$$

where $\boldsymbol{f}_\mathrm{jk}$ is the force density acting at node j due to node k, $\boldsymbol{f}_\mathrm{kj}$ is the force density acting at node k due to node j, and ΔV refers to the volume associated with a node (Ren et al. 2016). The force densities are illustrated in Fig. 2. Because we can implement peridynamics as a mesh free method (Silling and Askari 2005), it is feasible to adjust the number of nodes mid-simulation, apply local algorithmic rules at the node, and regularly update the connectivity between nodes. In the context of simulating cell population growth, this feature makes it possible to approximate mechanical mechanisms on the cellular scale, such as the cell division mechanism discussed in Sect. 2.3.

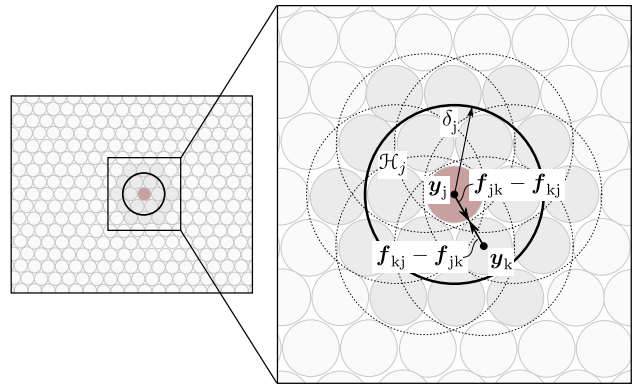

Fig. 2 Nodal position $\boldsymbol{y}_\mathrm{j}$, interaction distance δ_j, and horizon $\mathcal{H}_\mathrm{j}$ at node j in a peridynamic simulation. Force densities $\boldsymbol{f}_\mathrm{jk}$ and $\boldsymbol{f}_\mathrm{jk}$ arise due to interactions between node j and node k

In this approach, we choose a state-based peridynamic linear elastic solid with a growth term as the constitutive law for computing $\boldsymbol{f}$. The details of implementing this constitutive law in the discrete setting are included in Appendix A. Here, we briefly discuss strain energy density W and pressure p because these quantities are plotted in Sect. 3 to interpret simulation results. First, strain energy density is defined as

$$W_j = \frac{\kappa \theta_\mathrm{j}^2}{2} + \frac{n\,(n+2)\,\mu}{2 m_\mathrm{j}} \sum_{\mathrm{k}\in\mathcal{H}_\mathrm{j}} \omega_\mathrm{jk}\, (e_\mathrm{jk}^d)^2\, \Delta V_\mathrm{k} \tag{5}$$

where θ is dilation (isochoric deformation), $n = 3$ is the dimension, m is horizon weighted volume, κ and μ are Lamé parameters, ω is an influence function that is equal to zero if bonds are severed and one otherwise, and e^d is the deviatoric bond elongation fully defined in Appendix A (Silling et al. 2007). Pressure p is simply defined as

$$p_\mathrm{j} = -\kappa \theta_\mathrm{j} \tag{6}$$

where dilation θ depends radial growth g through parameter

$$\xi_\mathrm{jk} = (1 + g_\mathrm{j})\, r_\mathrm{j} + (1 + g_\mathrm{k})\, r_\mathrm{k} \tag{7}$$

and is written as

$$\theta_\mathrm{j} = \frac{n}{m_\mathrm{j}} \sum_{\mathrm{k}\in\mathcal{H}_\mathrm{j}} \omega_\mathrm{jk}\, \xi_\mathrm{jk}\, e_\mathrm{jk}\, \Delta V_\mathrm{k} \tag{8}$$

where e is bond elongation, again defined in Appendix A. With this basic mechanical framework in place, we now define growth rules controlling the progression of g and algorithmic rules to define cell division.

2.2 Homogeneous, noisy, and stress-limited growth rules

In our model, we define growth g as an increase in node radius that enters the constitutive law through Eq. (7). Cells (nodes) will first grow according to some algorithmic growth law and then divide when their radius exceeds a threshold size, described in Sect. 2.3. Homogeneous growth is defined as a uniform fractional increase in the volume of every cell. Specifically, some incremental fractional volume increase is defined as g_v^{inc} and used to update the growth of each cell from g^t to g^{t+1} as

$$g^{t+1} = (1 + g^t)(1 + g_v^{\text{inc}})^{1/3} - 1\,. \tag{9}$$

If the growth law in Eq. (9) is implemented, a population of cells arising from a single cell will all grow and divide perfectly in sync. However, real biological systems do not behave this way. The behavior of growing cells is highly stochastic, and populations of cells do not typically grow and divide perfectly in unison (Keyomarsi et al. 1991). Therefore we also introduce an alternative growth law that we refer to as noisy homogeneous growth. To do this, we introduce a random variable X and define g^{inc} with a new randomly determined value of X at every node. The growth update rule at node i is then written as

$$\begin{aligned} &\mathbb{P}(X = 1) = \mathbb{P}(X = -1) = \frac{1}{2} \\ &g^{\text{inc}} = \frac{1}{2}[(1 + g_v^{\text{inc}})^{1/3} - 1](1 + X) \\ &g^{t+1} = (1 + g^t)(1 + g^{\text{inc}}) - 1\,. \end{aligned} \tag{10}$$

This growth law is homogeneous in the sense that it does not depend on any spatial or temporal information. However, it can lead to neighboring cells with different levels of growth thereby introducing local inhomogeneity and a nontrivial mechanical microenvironment (Fig. 3).

In Sect. 3.3, we investigate the effects of a stress-limited growth law. There are multiple plausible forms that such a growth law may take (Ambrosi et al. 2011). Here we choose a simple form which prescribes zero growth whenever a cell experiences a level of compression below some threshold, motivated by the fact that compressive stresses are known to suppress growth (Helmlinger et al. 1997). With the peridynamic linear elastic constitutive law, isochoric stress is computed as a function of dilation θ (Eq. 8), and we implement our stress-suppressed zero growth law by prescribing zero growth, $g^{\text{inc}} = 0$, if p exceeds some threshold $p_{\max}$. Following the same random walk strategy as Eq. (10), we implement a "noisy" version of this growth law. The noisy stress-suppressed growth law is written as

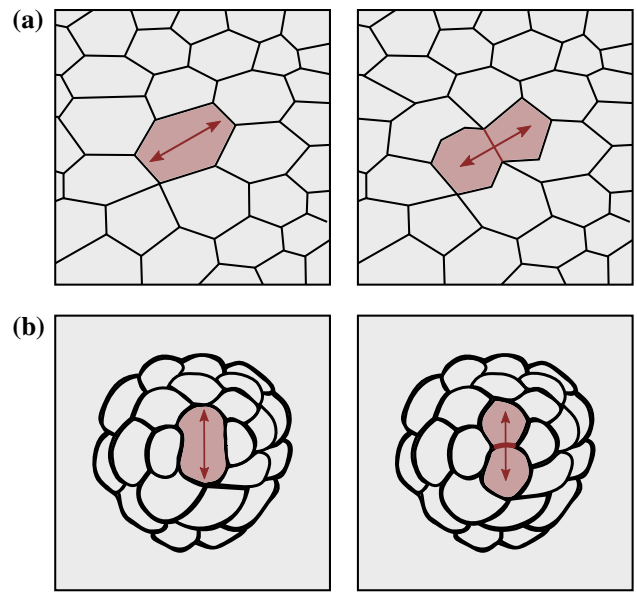

Fig. 3 **a** Illustration of cells dividing following the "long axis rule" in the 2D setting; **b** Illustration of cells dividing following the "long axis rule" in the 3D setting. In our simulations, we assume that a cell will only deviate from a spherical shape due to mechanical stress

$$\begin{aligned} &\mathbb{P}(X = 1) = \mathbb{P}(X = -1) = \frac{1}{2} \\ &p = -\kappa\theta \\ &g^{\text{inc}} = 0 \quad \text{if} \quad p > p_{\max} \quad \text{or} \quad X = -1. \end{aligned} \tag{11}$$

With stress-suppressed growth, spatially inhomogeneous growth patterns may emerge because the mechanical microenvironment within a growing monolayer and a growing spheroid are, on average, position dependent. This phenomena is explored in Sect. 3.3.

2.3 Cell division and the "long axis rule"

In addition to increases in cell size, population growth is driven by cell division (Gillies and Cabernard 2011). In our model, cell division occurs when a cell has grown enough to double in size. Specifically, given some initial cell volume $V_0 = \frac{4}{3}\pi r_0^3$, and current cell volume $V_t = \frac{4}{3}\pi[(1 + g^t)r_0]^3$, cells will divide when $V_t \geq 2V_0$. In order to prevent numerical problems, even homogeneously growing cells do not all divide in the same load step. Instead, cells divide in a random order and cell division occurs within a narrow threshold above and below $V_t = 2V_0$. When a cell divides, the associated node gives rise to two daughter nodes, initially forming a barbell shape prior to fully splitting into two spheres. After dividing, the equal growth of the two daughter cells g_d is computed as a function of the growth of the parent cell g_p

$$g_d = \sqrt[3]{\frac{1}{2}}(1 + g_p) - 1 \tag{12}$$

and the new spatial position of the two cells is computed as

$$\begin{aligned} \boldsymbol{y}_{\mathrm{j}} &= \boldsymbol{y}_0 + (1+g_d)\, r_0\, \boldsymbol{m} \\ \boldsymbol{y}_{\mathrm{k}} &= \boldsymbol{y}_0 - (1+g_d)\, r_0\, \boldsymbol{m} \end{aligned} \tag{13}$$

where $\boldsymbol{y}_0$ is the position of the parent cell before division occurs, r_0 is the initial cell radius without growth, and $\boldsymbol{m}$ is a unit vector representing division angle orientation. Division angle may depend on local factors such as chemical signals (Lamb et al. 2014), stretch (Wyatt et al. 2015), force (Nestor-Bergmann et al. 2014), cell geometry (Su et al. 2015), and cell packing geometry (Gibson et al. 2011). And, often division angle is best described as a stochastic quantity (Minc and Piel 2012; Minc et al. 2011; Théry et al. 2007).

Here, we consider two potential forms of $\boldsymbol{m}$. First, in the absence of any control, $\boldsymbol{m}$ can be expressed as unit vector with a random orientation. When the cell population is growing and dividing as a monolayer, the two-dimensional case, $\boldsymbol{m}$ is a random unit vector in the x-y plane conveniently computed in the algorithmic setting as

$$\theta := \mathcal{U}[0, 2\pi] \quad \boldsymbol{m} = [\,\sin\theta,\ \cos\theta\,,\ 0\,]. \tag{14}$$

In the three-dimensional case, this leads to a random unit vector in three-dimensional space conveniently computed in the algorithmic setting as

$$\begin{aligned} &\theta := \mathcal{U}[0, 2\pi] \qquad\qquad u := \mathcal{U}[-1, 1] \\ &\boldsymbol{m} = [\,\sqrt{1-u^2}\cos\theta,\ \sqrt{1-u^2}\sin\theta\,,\ u\,]. \end{aligned} \tag{15}$$

Alternatively, we can formulate $\boldsymbol{m}$ based on the local mechanical microenvironment. Specifically, one mechanically relevant choice for $\boldsymbol{m}$ is the "long axis rule." The "long axis rule" states that the plane of cell division will be orthogonal to the cell's long axis (Hertwig 1884). From a mechanics perspective, this rule is particularly compelling because controlling the orientation of cell division in proliferating cells can lead to cellular re-arrangements that dissipate stress (Ambrosi et al. 2012). In continuum modeling, the formulation of a phenomenological anisotropic growth law is often justified by the cellular scale division orientation and by the mechanically driven reorganization of dividing cells (Araujo and McElwain 2004).

In our model, where each cell is treated simply as a node with an associated radius, we assume that the best approximation of the cell's long axis is the direction of maximum principle stress computed at the corresponding node. In a previous study of the division angle that dismissed a stress-based division orientation in favor of the "long axis rule", stress-based division orientation was based on the global direction of maximum applied stress, rather than on the local direction of maximum stress within a cell (Wyatt et al. 2015). Stress does not naturally enter the peridynamic framework presented in Sect. 2.1; however, a similar quantity can be computed in a post-processing step as

$$\begin{aligned} \boldsymbol{s}_{\mathrm{j}} = &\frac{1}{2}\Big[\sum_{\mathrm{k}\in\mathcal{H}'_{\mathrm{j}}} \boldsymbol{f}_{\mathrm{jk}}(\boldsymbol{y}_{\mathrm{j}}, \boldsymbol{y}_{\mathrm{k}})\,\Delta V_{\mathrm{k}}\Big] \otimes \big[\boldsymbol{y}_{\mathrm{k}} - \boldsymbol{y}_{\mathrm{j}}\big] - \\ &\frac{1}{2}\Big[\sum_{\mathrm{k}\in\mathcal{H}_{\mathrm{j}}} \boldsymbol{f}_{\mathrm{kj}}(\boldsymbol{y}_{\mathrm{j}}, \boldsymbol{y}_{\mathrm{k}})\,\Delta V_{\mathrm{k}}\Big] \otimes \big[\boldsymbol{y}_{\mathrm{k}} - \boldsymbol{y}_{\mathrm{j}}\big] \end{aligned} \tag{16}$$

where $\boldsymbol{s}_{\mathrm{j}}$ is the stress equivalent at node j where index k represents all of the nodes in the horizon and dual horizon of node j (Silling and Lehoucq 2010). In the two-dimensional case, we compute $\boldsymbol{s}$ as two dimensional in the x-y plane. To approximate the "long axis", we first compute the directions of maximum principle stress where λ_1 and λ_2 are the eigenvalues of $\boldsymbol{s}$ from largest to smallest, with the largest corresponding to the direction of highest tension, and $\boldsymbol{v}_1$ and $\boldsymbol{v}_2$ are the associated unit eigenvectors. If $\lambda_1 \approx \lambda_2$ within machine precision, $\boldsymbol{m}$ is assigned a random orientation in the x-y plane. We assign $\boldsymbol{m}$ following the statement

$$\begin{aligned} &\text{if} \quad \lambda_1 \approx \lambda_2 \quad \text{then} \quad \theta := \mathcal{U}[0, 2\pi] \\ &\quad \boldsymbol{m} = [\,\cos\theta, \sin\theta\,] \\ &\text{if} \quad \lambda_1 > \lambda_2 \quad \text{then} \quad \boldsymbol{m} = \boldsymbol{v}_1\,. \end{aligned} \tag{17}$$

In the three-dimensional case, we compute λ_1, λ_2 and λ_3 as the eigenvalues of $\boldsymbol{s}$ from largest to smallest and $\boldsymbol{v}_1$, $\boldsymbol{v}_2$ and $\boldsymbol{v}_3$ as the associated unit eigenvectors. If $\lambda_1 \approx \lambda_2 \approx \lambda_3$ within machine precision, $\boldsymbol{m}$ is assigned as a random orientation in three-dimensional space. If $\lambda_1 \approx \lambda_2$, vector $\boldsymbol{m}$ is placed randomly in the plane defined by $\boldsymbol{v}_1$ and $\boldsymbol{v}_2$. This is implemented by defining rotation matrix $\boldsymbol{R}$ from the eigenvectors. If $\lambda_1 > \lambda_2$ then $\boldsymbol{m} = \boldsymbol{v}_1$. Overall, we assign $\boldsymbol{m}$ as

$$\begin{aligned} &\text{if} \quad \lambda_1 \approx \lambda_2 \approx \lambda_3 \quad \theta := \mathcal{U}[0, 2\pi] \quad u := \mathcal{U}[-1, 1] \\ &\quad \boldsymbol{m} = [\,\sqrt{1-u^2}\cos\theta\,,\ \sqrt{1-u^2}\sin\theta\,,\ u\,] \\ &\text{if} \quad \lambda_1 \approx \lambda_2 \quad \boldsymbol{R} = [\boldsymbol{v}_1\, \boldsymbol{v}_2\, \boldsymbol{v}_3] \quad \theta := \mathcal{U}[0, 2\pi] \\ &\quad \boldsymbol{m} = \boldsymbol{R}^{-1} \cdot [\,\cos\theta\,,\ \sin\theta\,,\ 0\,] \\ &\text{if} \quad \lambda_1 > \lambda_2 \quad \boldsymbol{m} = \boldsymbol{v}_1\,. \end{aligned} \tag{18}$$

More complex realizations of the "long axis rule" that take into account sub- cellular effects and additional stochastic components are potentially justified (Bosveld et al. 2016; Akanuma et al. 2016), but beyond the scope of this paper. Further distinction between the two-dimensional and three-dimensional case beyond algorithmic rules guiding the orientation of cell division $\boldsymbol{m}$ is made in Sect. 2.4.

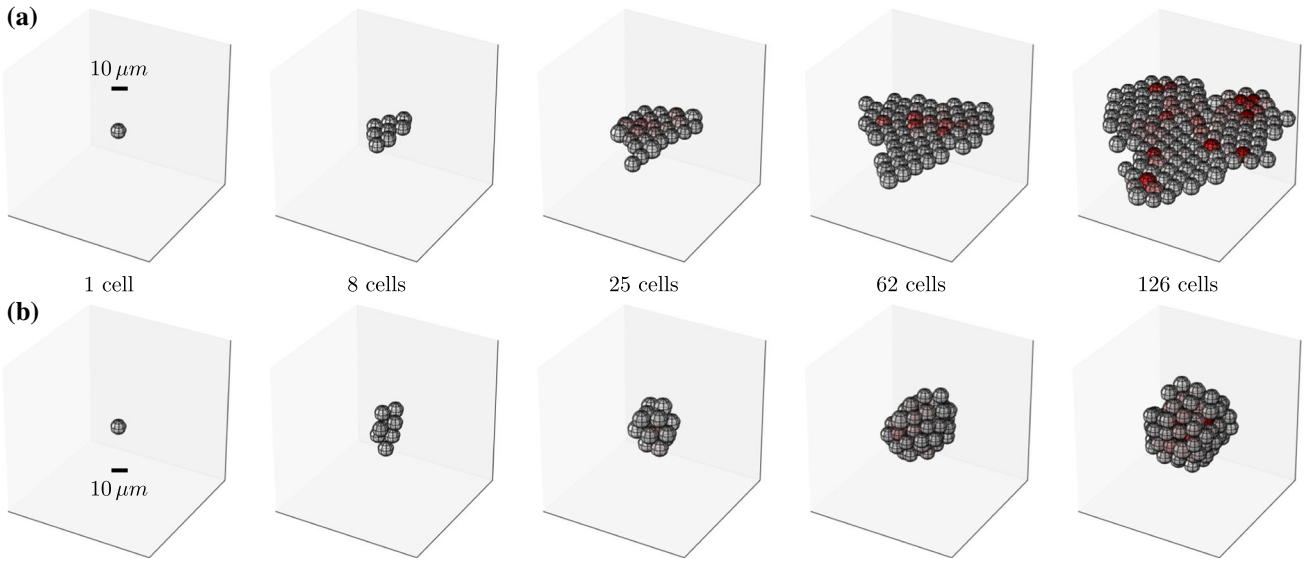

Fig. 4 **a** Cells constrained to divide in the x–y plane form a monolayer; **b** Unconstrained cells form a spheroid. In both cases, red color corresponds to strain energy density (W) at the node, with gray corresponding to $W = 0$. Cells are visualized as perfect spheres with diameter proportional to cell growth

2.4 Two-dimensional and three-dimensional simulations

In Fig. 4, an example of two single simulations conducted with the agent-based model are shown. The input parameters to both simulations are entirely identical except that in the upper row, cells are restricted to divide in the x–y plane, while in the lower row, there are no restrictions on the orientation of cell division. This restriction of cell division orientation to the x-y plane is enough to ensure that the population maintains a monolayer. However, without an additional boundary condition, this configuration is geometrically unstable and a small perturbation will cause the sheet to collapse out of plane. To avoid this instability in all simulations intended to be two dimensional, we simply impose a condition of zero deformation in the z-direction. This boundary condition, combined with in-plane cell division, is physically similar to the presence of a stabilizing substrate where the time scale of the resistance to sliding at the cell-substrate interface is much shorter than the time scale of cell proliferation. In the case of no boundary conditions and no dimensional restrictions on division orientation, proliferating cells form spheroids, shown in the lower row of Fig. 4. Individual simulations, like the ones illustrated in Fig. 4, are stochastic; therefore, it is necessary to run multiple simulations to get a clear picture how different algorithmic rules actually influence overall population behavior. In Sect. 3, we present results from running thousands of simulations.

3 Results and discussion

Given the general framework presented in Sect. 2, we investigate three fundamental aspects of the mechanics of growing monolayers and spheroids. First, in Sect. 3.1, we compare synchronized and unsynchronized growth, and randomly oriented and "long axis rule" oriented division, and determine which combination results in the lowest average strain energy density per cell. Second, in Sect. 3.2, given a spatially homogeneous growth rule and cell division algorithm, we investigate the spatial distribution of strain energy density and isochoric stress in an average cell population. Third, in Sect. 3.3, we study a growth law where growth is suppressed when stress exceeds a certain threshold. In Table 2, we list the parameters used to implement the results presented in this section. From examining the results of thousands of simulations, patterns arise which enhance our understanding of proliferating cell populations in the two-dimensional and three-dimensional case.

3.1 Comparison of cell growth and division algorithms for the homogeneous growth case

In Sect. 2.2, we specified two potential homogeneous growth rules. First, a homogeneous growth update rule defined by Eq. (9), and second, a noisy homogeneous growth update rule defined by Eq. (10). In Sect. 2.3, we specified two cell division orientation algorithms. First, a random division algorithm defined by Eq. (14) in monolayers and Eq. (15) in spheroids, and second a "long axis rule" division algorithm defined by Eq. (17) in monolayers and Eq. (18) in

Table 2 This table summarizes the parameters selected for simulation

Parameter	Value	Source
E	1 kPa	Plausible value
ν	0.45	Nearly incompressible material
r_0	5 µm	Standard value (Drasdo and Höhme 2005)
$s_{\max}$	1.15	Reliably include nearest neighbors (Lejeune and Linder 2017a)
δ_0	1.15	Reliably include nearest neighbors (Lejeune and Linder 2017a)
$p_{\max}$	0.33 kPa	Threshold value chosen to exceed average p computed in Sect. 3.2

In Sect. 3, we report results in dimensionless form when possible because there is a range of reasonable values that could be selected to describe the material properties of biological cells (Guz et al. 2014)

spheroids. In this section, we aim to quantitatively compare the four potential combinations of growth and division rules described by these equations. One meaningful way to compare cases is to consider the average strain energy density per cell W defined by Eq. (5). By comparing average W with respect to simulation progression, it is possible to identify which combination of rules allows the population of cells to grow and divide in as close to a stress and strain free state as possible. In Fig. 5, we plot average W with respect to total normalized cell population volume for all four combinations in both the two-dimensional and three-dimensional cases. Each curve represents the average of 200 simulations.

From the results in Fig. 5, it is clear that in both the two-dimensional and three-dimensional case, the rule combination with the consistently lowest average strain energy density is the noisy homogeneous growth rule paired with the "long axis rule" for cell division orientation (n.h.g; l.a.d). In all curves plotted in Fig. 5, average W spikes when a high number of cell division events are occurring simultaneously as cells are forced to re-arrange and may become jammed. When growth is "noisy" cells do not divide in sync, therefore these peaks are lower and more spread out. Compared to random division, the "long axis rule" division also lowers average W. This observation confirms intuition that the "long axis rule" may be a relevant mechanism for dissipating stress. In comparing the two-dimensional and three-dimensional cases, the results are qualitatively similar, although in the three-dimensional case average W is higher, which makes sense because each cell, on average, interacts with more cells within its horizon than in the two-dimensional case therefore increasing the number of terms contributing to W. Finally, as the number of cells increases, average W increases slightly in all cases, though this effect is much more pronounced in the case of homogeneous growth with random division. Next, in Sect. 3.2, we present additional simulation results from the noisy homogeneous growth rule combined with the "long axis rule" division orientation rule. Moving forward, we focus on the cases that correspond to lower W under the assumption that they are more likely to occur in real biological systems.

3.2 Spatial distribution of strain energy density and isochoric stress for the homogeneous growth case

In Sect. 1, we emphasize that predicting the spatial distribution of stress within a growing tumor spheroid is not

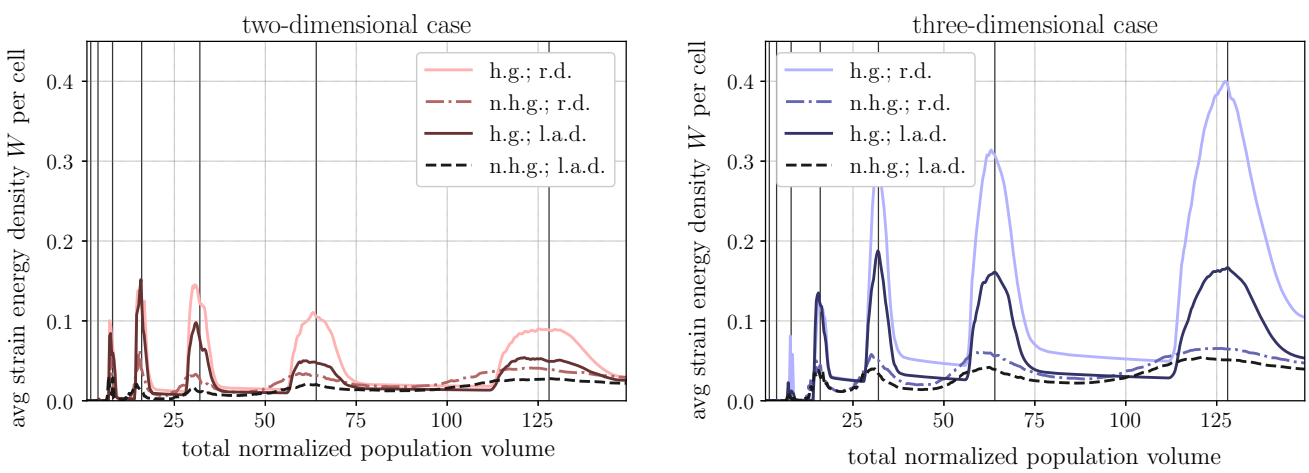

Fig. 5 Average strain energy density, W per cell (kPa) with respect to the total cell population volume normalized by the volume of a single cell with $g = 0$. Each curve represents the average of 200 simulations. The growth rules referred to in the legend are "homogeneous growth" (h.g.) following Eq. (9), "noisy homogeneous growth" (n.h.g.) following Eq. (10), "random division" (r.d.) following Eqs. (14) and (15), and "long axis division" (l.a.d.) following Eqs. (17) and (18). In both plots, peaks occur when there are a large number of cell division events occurring

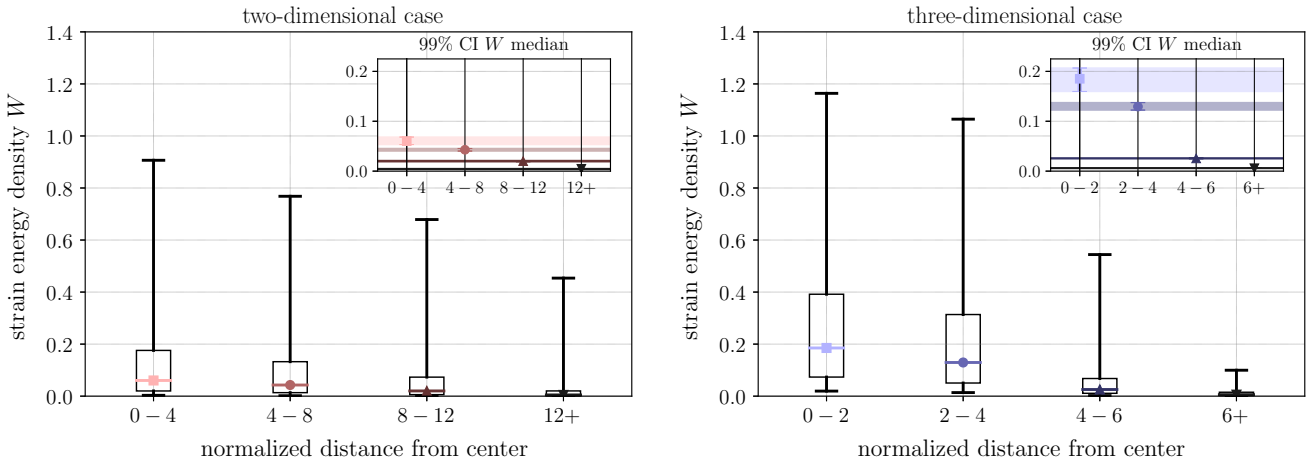

Fig. 6 Spatial distribution of W (kPa) at the end of the simulation for 200 two-dimensional and 200 three-dimensional stochastic simulations. Growth is unsynchronized following Eq. (10), and cell division orientation is determined by the "long axis rule" following Eqs. (17) and (18). In the box plots, the box covers 50% of the data while the whiskers cover 95%. The inset plots show the bootstrap confidence interval around the medians of each distance group. From these plots, it is clear that the values of p are highly variable, and they increase toward the population center

trivial. With mechanically robust agent-based modeling, it is possible to explore the spatial distribution of stress within monolayers and spheroids including stochastic fluctuations. In the continuum setting, this exploration would not be straightforward. With our agent-based model, we are able to make explicit modeling choices on the cellular scale and subsequently examine their implications on the population scale. This contrasts with the approach of assigning phenomenological rules from the macro-scale regime. The spatial distributions of nodal strain energy density W and isochronic stress p are plotted for both the two-dimensional and three-dimensional case in Figs. 6 and 7, respectively. Notably, in both cases, the average magnitude of strain energy density W increases closer to the population center, and in both cases there is a large degree of stochastic fluctuation throughout. A single simulated population may include both cells where $W \approx 0$ and cells with nontrivial values of W. By looking at the combined results of 200 simulations in each the two-dimensional and three-dimensional case, we see a pattern of higher W toward the population center. This result is reasonable because for cells close to the population edge, there is nothing preventing them from freely shifting and deforming outward, while for the cells close to the population center, motion is constrained by surrounding neighbors. Furthermore, when comparing monolayers and spheroids, it is clear that W is on average higher in the three-dimensional case, consistent with the results reported in Fig. 5.

In addition to examining the spatial distribution of strain energy density, we also explore the spatial distribution of isochoric stress p. Here, a positive value of p corresponds to compression. Consistent with the spatial distribution of W, the average magnitude of p is higher in the population center than at the population edges. In the monolayer case, average p is close to zero throughout the domain, with a slight increase toward the center. Throughout the interior of the domain, cells experience non-zero isochoric stress, with the number of cells in tension approximately equal the number of cells in compression. Returning to the problem of freely growing avascular tumor spheroids discussed in Sect. 1, we are now prepared to comment on what our model predicts as the stress state in the interior of a tumor spheroid, i.e. the three-dimensional case. Consistent, both mechanistically and in the outcome, with the results predicted in Drasdo and Höhme (2005), our model predicts that cells in the center of a tumor spheroid will, on average, experience compression because as they divide and re-arrange they become "jammed" by their neighbors. In the three-dimensional case cells become more easily "jammed" than in the monolayer case. Beyond average behavior, our results also show that there will be sufficient stochastic fluctuation in p such that at an instant in time cells in the population interior may experience either tension or compression. This is significant because there are several plausible nonlinear interactions between stress state and growth law. For example, cells that experience higher levels of tension may divide at a faster rate, while cells that experience higher levels of compression may not be able to grow further or may undergo apoptosis. The lower magnitudes of stress observed toward the monolayer and spheroid peripheries are a potential explanation for faster relative growth at the population edge. The results of implementing a growth law chosen to show the importance of this stress distribution and the observed stochastic fluctuations are presented in

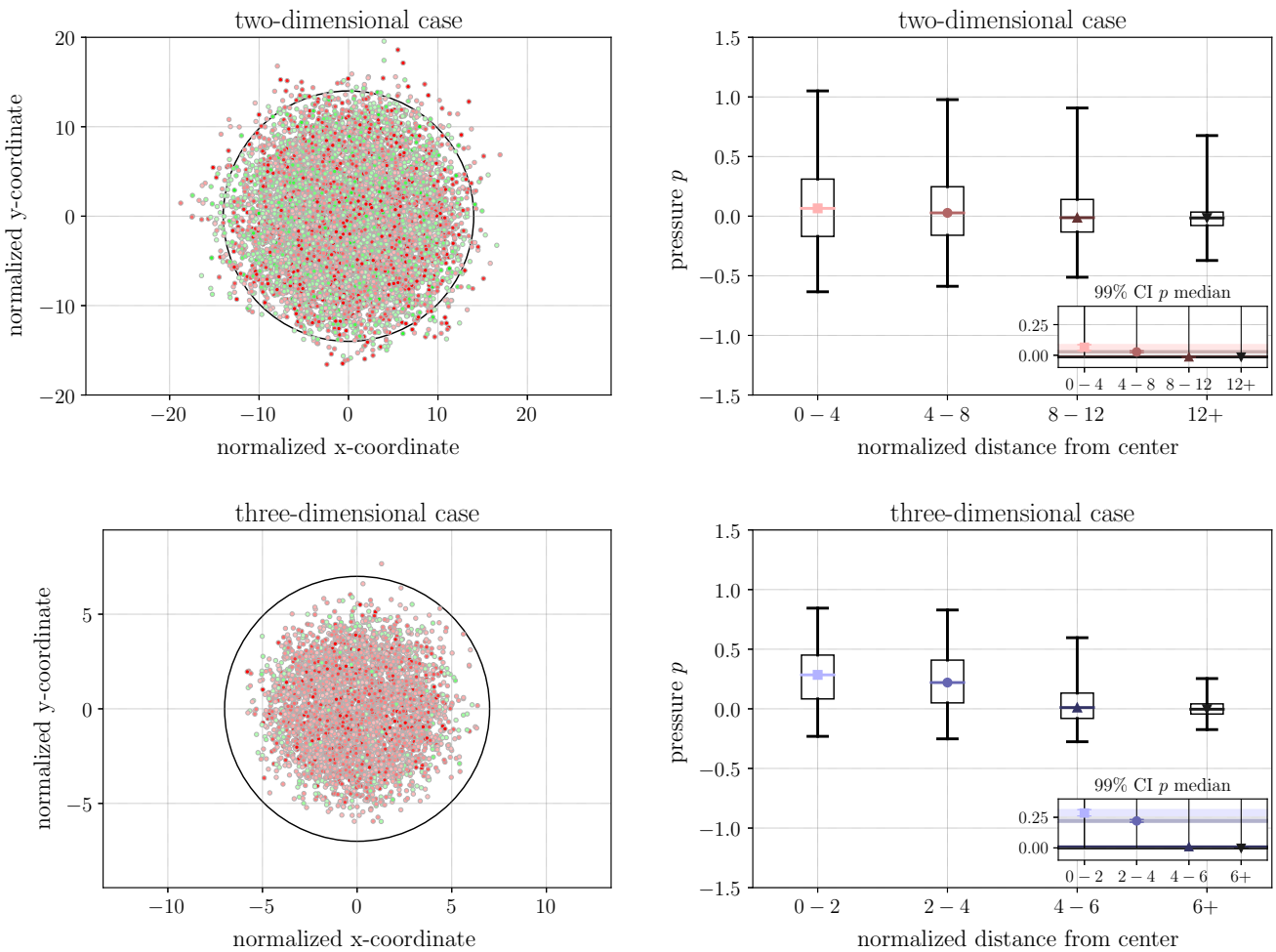

Fig. 7 Spatial distribution of p (kPa) at the end of the simulation for 200 two-dimensional and 200 three-dimensional stochastic simulations. Growth is unsynchronized following Eq. (10), and cell division orientation is determined by the "long axis rule" following Eqs. (17) and (18). In the scatter plots, nodes that fall within a slice through the x-y plane are plotted. Red color indicates $p > 0.25$, green color indicates $p < -0.25$, and all points with $-0.25 < p < 0.25$ are omitted. The circles indicate the approximate outline of a typical cell population. Within this outline, empty areas have few cells with larger values of p. In the box plots, the box covers 50% of the data, while the whiskers cover 95%. The inset plots show the bootstrap confidence interval around the medians of each distance group. From these plots, it is clear that the values of p are highly variable. In the three-dimensional case, p tends to increase significantly toward the population center, indicating compression

Sect. 3.3. Other combinations of growth and division rules from Sect. 3.1 yield qualitatively similar results, with higher strain energy density toward the cell population center than the edges, although quantitatively the magnitudes of W and of p are larger. This qualitative trend persists throughout the course of population growth.

3.3 The stress-suppressed growth case

In Sect. 3.2, we examined the spatial distributions of strain energy density and isochoric stress in a growing and dividing cell population with a noisy homogeneous growth rule. In this section, we consider the case where the growth update rule is defined by Eq. (11) with growth suppressed when p exceeds some critical threshold set as $p_{\max} = 0.33$. This threshold was chosen such that it is greater than the median value of compression close to the tumor spheroid center reported in Sect. 3.2. If stochastic fluctuations in p were not explicitly captured by this model, this choice of growth rule would be no different from the noisy homogeneous growth rule. The stress-suppressed growth law results in spatially inhomogeneous growth because of the spatial variability of the distribution of p. Specifically, p tends to be higher toward the center of the population, which means that growth is more likely suppressed in that region. In Fig. 8, the results of implementing this growth rule are summarized. In total, 400 simulations were conducted, 200 for each the two-dimensional and three-dimensional case. Based on

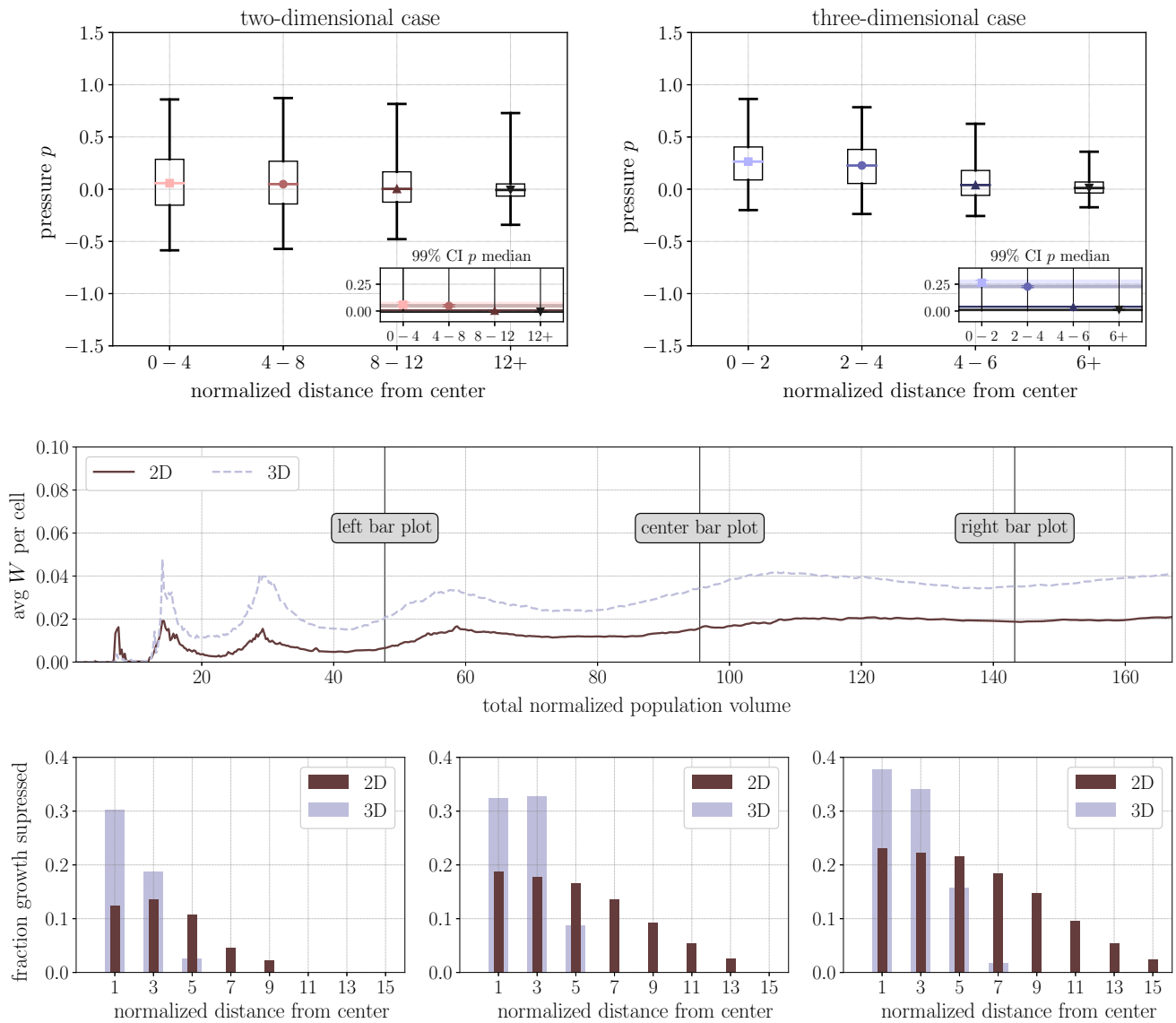

Fig. 8 Spatial distribution of p (kPa) at different points in the simulation for 200 two-dimensional and 200 three-dimensional stochastic simulations. Growth is unsynchronized and suppressed when the cell experiences isochoric stress p above a certain threshold following Eq. (11), and cell division orientation is determined by the "long axis rule" following Eqs. (17) and (18). In the box plots, p (kPa) is plotted. The box covers 50% of the data, while the whiskers cover 95%. The inset plots show the bootstrap confidence interval around the medians of each distance group. Figure 9 in Appendix B contains identical plots for different instances throughout the simulation. In the line plot, average strain energy density W (kPa) per cell is plotted with respect to the total population volume normalized by the volume of a single cell with $g = 0$. In the bar plots, the fraction of growth suppressed cells is plotted with respect to normalized distance from center. Notably, the three-dimensional cases lead to more growth suppression

the plots in the upper row of Fig. 8, it is clear that the spatial distribution of p is qualitatively and quantitatively similar to the spatial distribution of p for the homogeneous growth rule presented in Fig. 7. The second row of Fig. 8 shows the change in average W per cell with respect to normalized total population volume for both the two-dimensional and three-dimensional cases. The magnitudes of average W are similar to the magnitudes of average W for the noisy homogeneous growth with "long axis rule" division orientation presented in Fig. 5. The final row of plots in Fig. 8 shows the spatial distribution of stress suppression in both the two-dimensional and three-dimensional cases. Each bar in the bar chart approximately represents one shell layer of cells. Clearly, the stress suppression of growth increases toward the cell population center.

From all of the results presented in Figs. 5–8, it is clear that the mechanical microenvironments of monolayers and spheroids are distinct. Specifically, the stress caused by

local inhomogeneities and cell "jamming" is higher in the three-dimensional case, and on average the population center experiences higher compression. In Fig. 8c, one potential implication of this difference is highlighted. The bar graphs show that when growth is suppressed by mechanical stress, the effects will be greater in the spheroid case. This shows that even for small population sizes, where nutrient deficiencies are most likely not relevant, the difference in mechanical microenvironment may cause noticeable spatially distributed changes in cell proliferation rate and differences between two-dimensional and three-dimensional culture conditions. This result is qualitatively similar to results reported in the experimental literature (Price et al. 2017).

In the three-dimensional case, we also consider the results of this study in the context of a growing tumor spheroid. Even without a nutrient dependent component, the stress-dependent growth law is sufficient to cause differential growth rates in different layers of the growing spheroid. Similar to the differential growth that would be induced by a nutrient dependent growth law (Ambrosi and Mollica 2002), our mechanically dependent growth law leads to an outer layer that grows faster than the inner core. However, unlike many results reported in the literature, see for example Table 1, this does not lead to tension in the inner core of the spheroid. By using agent-based modeling, where cell growth and cell division are explicitly separate mechanisms, we instead observe compression in the spheroid center. The results in Fig. 8 show that isochoric stress increases from nearly zero on the spheroid surface to a higher value on average toward the center of the spheroid with large stochastic fluctuations. By approaching this problem with an agent-based model, we are able to capture these stochastic fluctuations and gain a better understanding of the stress state that emerges due to cell division and rearrangement in a tumor spheroid.

4 Conclusion

The main objective of this work is to explore residual stresses in a growing populations of cells using a mechanically robust agent-based model. Our results indicate that even within an unconstrained population of homogeneously growing cells, stress arises when the cell division mechanism is accounted for. In Sect. 3.1, we showed that a noisy homogeneous growth rule with cell division according to the "long axis rule" results in the lowest average strain energy density per cell compared to random division and synchronized growth. In Sect. 3.2, we examined the spatial distribution of strain energy density and isochoric stress in a growing population of cells. In Sect. 3.3, we tested a growth law where growth was suppressed by compressive isochoric stress above a certain threshold. And, in all three sections, we compare monolayers and spheroids, and note the quantitative and qualitative differences between the resulting mechanical microenvironments. In all cases, strain energy density is, on average, higher in the three-dimensional case. And, in the three-dimensional case, average isochoric compressive stresses at the population center are higher than in the two-dimensional case. These quantitative differences may help explain some of the experimentally observed variability in cell behavior between two-dimensional and three-dimensional cell culture. By studying growing spheroids, we can also compare our results to results obtained with other models in the literature. Our model predicts compressive stress in the center of a freely growing tumor spheroid. Finally, we emphasizes the importance of accounting for stochastic fluctuations in stress in a growing population of cells. We believe that future models of growing and dividing cell populations formulated on the continuum scale should not ignore these fluctuations and the potential nonlinear effects that may be triggered by them.

It is also worth mentioning that the computational methods presented in Sect. 2 are quite general, and can be used as a starting point for additional investigation. For example, the simulation framework used for comparing growth and division laws with results reported in Sect. 3.1 is a strategy for choosing the appropriate algorithmic rules to implement in an agent-based model under the assumption that the most likely algorithms for cell growth and division are those that are on average as close to "stress free" as possible. Future work with this framework may address topics such as the influence of nutrient availability regulated growth, cell migration, cell death, viscoelasticity and more complex material response, explicit substrate boundary conditions, and the possibility of cell differentiation. Investigating the case of an avascular tumor spheroid embedded in a deformation resisting biologically responsive media is also a natural next step. For the move toward modeling residual stresses in real tumors, it will be necessary to incorporate the effects of swelling driven by extracellular matrix components (Lai et al. 2016; Voutouri et al. 2016). Finally, given that agent-based models are limited to cell populations of a relatively small size, we also anticipate that one of the main utilities of further investigation will be to inform the construction of continuum models either through improving phenomenological models or as a part of a multiscale framework. Insight gained from agent-based models will lead to tissue and organ scale models that manage to robustly account for different cell division and cellular scale growth rules, and properly capture the stochastic fluctuations observed in models constructed on the cellular scale.

Acknowledgements We would like to thank Claudia Vasquez, Andrew Price, Vipul Vachharajani, and Alex Dunn for the stimulating discussions and helpful comments.

Funding This work was supported by the National Science Foundation Graduate Research Fellowship under Grant No. DGE-114747.

Compliance with ethical standards

Conflicts of interest The authors declare that they have no conflict of interest.

A Mechanical model implementation

Variable	Meaning
ρ	Density
$\ddot{\boldsymbol{u}}$	Acceleration
$\boldsymbol{x}$	Particle reference
$\boldsymbol{f}_{\boldsymbol{x}\boldsymbol{x}'}$	Force per volume acting on particle $\boldsymbol{x}$ due to particle $\boldsymbol{x}'$
$\boldsymbol{f}_{\boldsymbol{x}'\boldsymbol{x}}$	Force per volume acting on particle $\boldsymbol{x}'$ due to particle $\boldsymbol{x}$
$\mathcal{H}_{\boldsymbol{x}}$	Horizon of particle $\boldsymbol{x}$
$\mathcal{H}'_{\boldsymbol{x}}$	Dual horizon of particle $\boldsymbol{x}$
$\boldsymbol{\xi}$	Particle separation distance vector
s	Stretch between particles
$s_{\max}$	Critical stretch
$\underline{e}$	Bond elongation
θ	Dilation
μ	Lamé parameter
κ	Lamé parameter
$V_{\boldsymbol{x}}$	Volume associated with particle $\boldsymbol{x}$
$\boldsymbol{b}$	Body force density
δ^0	Baseline horizon size
δ	Growth modified horizon size
g	Radial growth
$\boldsymbol{y}$	Current position of particle $\boldsymbol{x}$
n	Dimension, $n = 3$
r_0	Initial particle radius
γ	Bond damage
$\underline{\omega}$	Influence function
$\underline{e}^d$	Deviatoric bond elongation
$\underline{t}$	Magnitude of force density vector
W	Strain energy density
m	Weighted horizon volume

The fundamentals of the mechanical model used in this paper follow directly from references (Lejeune and Linder 2017a, b). In this section, we use the notation that is most consistent with the peridynamics literature. In the main body of this paper, we used a simplified notation. The correspondence between the two notation styles is made clear here.

The continuous version of the peridynamic equation of motion is as follows

$$\rho\ddot{\boldsymbol{u}}(\boldsymbol{x},t) = \int_{\boldsymbol{x}'\in\mathcal{H}'_{\boldsymbol{x}}} \boldsymbol{f}_{\boldsymbol{x}\boldsymbol{x}'}(\boldsymbol{y},\boldsymbol{y}')\,d V_{\boldsymbol{x}'} - \int_{\boldsymbol{x}'\in\mathcal{H}_{\boldsymbol{x}}} \boldsymbol{f}_{\boldsymbol{x}'\boldsymbol{x}}(\boldsymbol{y}',\boldsymbol{y})\,d V_{\boldsymbol{x}'} + \boldsymbol{b}(\boldsymbol{x},t) \tag{19}$$

where each particle experience forces from the other particles within the horizon defined by horizon size parameter δ written as

$$\delta_{\mathrm{j}} = 2(1+g_{\mathrm{j}})r_0\,\delta^0_{\mathrm{j}}\,. \tag{20}$$

The horizon is defined as

$$\mathcal{H}_{\mathrm{j}} = \{\mathrm{k}\,|\;\; ||\boldsymbol{y}_{\mathrm{k}} - \boldsymbol{y}_{\mathrm{j}}|| < \delta_{\mathrm{j}}\} \tag{21}$$

and the dual horizon is defined as

$$\mathcal{H}'_{\mathrm{j}} = \{\mathrm{k}\,|\;\; \mathrm{j}\in\mathcal{H}_{\mathrm{k}}\}\,. \tag{22}$$

Finally, growth-dependent volume is defined as

$$\Delta V_{\mathrm{j}} = (1+g_{\mathrm{j}})^n\,\Delta V_{\mathrm{j}}\,. \tag{23}$$

In the absence of body force, the static equilibrium discrete form of the equation of motion can be written as

$$0 = \sum_{\mathrm{k}\in\mathcal{H}'_{\mathrm{j}}} \boldsymbol{f}_{\mathrm{jk}}(\boldsymbol{y}_{\mathrm{j}},\boldsymbol{y}_{\mathrm{k}})\,\Delta V_{\mathrm{k}} - \sum_{\mathrm{k}\in\mathcal{H}_{\mathrm{j}}} \boldsymbol{f}_{\mathrm{kj}}(\boldsymbol{y}_{\mathrm{j}},\boldsymbol{y}_{\mathrm{k}})\,\Delta V_{\mathrm{k}}\,. \tag{24}$$

To define the force densities $\boldsymbol{f}$, we define the node separation distance as

$$\xi_{\mathrm{jk}} = ||\boldsymbol{\xi}_{\mathrm{jk}}|| = (1+g_{\mathrm{j}})r_{\mathrm{j}} + (1+g_{\mathrm{k}})r_{\mathrm{k}} \tag{25}$$

where ξ_{jk} is the simplified notation used in the main body of the text. Then, we define the stretch as

$$s = \frac{||\boldsymbol{y}_{\mathrm{k}} - \boldsymbol{y}_{\mathrm{j}}|| - ||\boldsymbol{\xi}_{\mathrm{jk}}||}{||\boldsymbol{\xi}_{\mathrm{jk}}||} \tag{26}$$

the bond damage as a function of stretch

$$\gamma(\boldsymbol{\xi}_{\mathrm{jk}},t) = \begin{cases} 1 & \text{if } s < s_{\max} \\ 0 & \text{otherwise} \end{cases} \tag{27}$$

and the influence function as

$$\omega_{\mathrm{jk}} = \underline{\omega}\langle\boldsymbol{\xi}_{\mathrm{jk}}\rangle = \gamma(\boldsymbol{\xi}_{\mathrm{jk}},t)\,. \tag{28}$$

Using these parameters, we define horizon weighted volume as

$$m_{\mathrm{j}} = \sum_{\mathrm{k}\in\mathcal{H}_{\mathrm{j}}} \underline{\omega}\langle\boldsymbol{\xi}_{\mathrm{jk}}\rangle\,||\boldsymbol{\xi}_{\mathrm{jk}}||^2\,\Delta V_{\mathrm{k}}\,. \tag{29}$$

Then, bond elongation is written as

$$e_{\mathrm{jk}} = \underline{e}\langle\boldsymbol{\xi}_{\mathrm{jk}}\rangle = ||\boldsymbol{y}_{\mathrm{k}} - \boldsymbol{y}_{\mathrm{j}}|| - ||\boldsymbol{\xi}_{\mathrm{jk}}|| \tag{30}$$

and dilation at every node is defined as

$$\theta_{\mathrm{j}} = \frac{n}{m_{\mathrm{j}}} \sum_{\mathrm{k} \in \mathcal{H}_{\mathrm{j}}} \underline{\omega}\langle \boldsymbol{\xi}_{\mathrm{jk}} \rangle \, ||\boldsymbol{\xi}_{\mathrm{jk}}|| \, \underline{e}\langle \boldsymbol{\xi}_{\mathrm{jk}} \rangle \, \Delta V_{\mathrm{k}} \, . \tag{31}$$

Using these parameters, we define deviatoric bond elongation as

$$e^{d}_{\mathrm{jk}} = \underline{e}^{d}\langle \boldsymbol{\xi}_{\mathrm{jk}} \rangle = \underline{e}\langle \boldsymbol{\xi}_{\mathrm{jk}} \rangle - \frac{\theta_{\mathrm{j}} ||\boldsymbol{\xi}_{\mathrm{jk}}||}{n} \, . \tag{32}$$

As stated in the main text, strain energy density is defined as

$$W_j = \frac{\kappa \theta_{\mathrm{j}}^{2}}{2} + \frac{n\,(n+2)\,\mu}{2 m_{\mathrm{j}}} \sum_{\mathrm{k} \in \mathcal{H}_{\mathrm{j}}} \underline{\omega}\langle \boldsymbol{\xi}_{\mathrm{jk}} \rangle \, (\underline{e}^{d}\langle \boldsymbol{\xi}_{\mathrm{jk}} \rangle)^{2} \, \Delta V_{\mathrm{k}} \tag{33}$$

and the magnitude of force density is computed from W as $\underline{t} = \partial W / \partial \underline{e}$ which results in

$$\underline{t}_{\mathrm{kj}}\langle \boldsymbol{\xi}_{\mathrm{jk}} \rangle = \frac{n\,\kappa\,\theta_{\mathrm{j}}}{m_{\mathrm{j}}} \underline{\omega}\langle \boldsymbol{\xi}_{\mathrm{jk}} \rangle ||\boldsymbol{\xi}_{\mathrm{jk}}|| + \frac{n\,(n+2)\,\mu}{m_{\mathrm{j}}} \underline{\omega}\langle \boldsymbol{\xi}_{\mathrm{jk}} \rangle \, \underline{e}^{d}\langle \boldsymbol{\xi}_{\mathrm{jk}} \rangle \, . \tag{34}$$

With magnitude $\underline{t}$ and direction based on the position of nodes in the current configuration the force density required to solve Eq. (24) is finally computed as

$$\begin{aligned} \boldsymbol{f}_{\mathrm{jk}}(\boldsymbol{y}_{\mathrm{j}}, \boldsymbol{y}_{\mathrm{k}}) &= \underline{t}_{\mathrm{jk}} \cdot \frac{\boldsymbol{y}_{\mathrm{k}} - \boldsymbol{y}_{\mathrm{j}}}{||\boldsymbol{y}_{\mathrm{k}} - \boldsymbol{y}_{\mathrm{j}}||} \\ \boldsymbol{f}_{\mathrm{kj}}(\boldsymbol{y}_{\mathrm{j}}, \boldsymbol{y}_{\mathrm{k}}) &= \underline{t}_{\mathrm{kj}} \cdot \frac{-(\boldsymbol{y}_{\mathrm{k}} - \boldsymbol{y}_{\mathrm{j}})}{||\boldsymbol{y}_{\mathrm{k}} - \boldsymbol{y}_{\mathrm{j}}||} . \end{aligned} \tag{35}$$

In Algorithm 1, the numerical solution algorithm, which connects the equations presented in Sect. 2 and the additional information in this Appendix, is given. Additional information on peridynamic theory and the numerical implementations of peridynamics is readily available in the literature (Madenci and Oterkus 2014; Silling and Lehoucq 2010; Littlewood 2015; Oterkus 2015).

Algorithm 1: Biological growth with peridynamics: numerical implementation procedure.

```
Input  : Initial node positions and properties, prescribed loading,
         prescribed cell division parameters
Output: Final node positions, final peridynamic forces.
for Load step t in prescribed loading do
    for Node j in node list do
        increment growth at each node g_j according to prescribed
        growth rule (either eqn. (9), eqn. (10) or eqn. (11))
    end
    for Node j in node list do
        if g_j > g_crit then
            begin cell division algorithm: separate parent node
            into two daughter nodes with m determined according
            to eqn. (14), eqn. (15), eqn. (17) or eqn. (18)
        end
    end
    while Nodes are not at mechanical equilibrium (i.e.
    acceleration ≥ ≈ 0) do
        for Node j in node list do
            Compute horizon H_j using eqn. (21)
        end
        for Node j in node list do
            Compute ω(ξ_jk) using eqn. (28) for every bond with
            node k in H_j
        end
        for Node j in node list do
            Compute m_j using eqn. (29) by looping through the
            nodes k in H_j
        end
        for Node j in node list do
            Compute θ_j using eqn. (31) by looping through the
            nodes k in H_j
        end
        for Node j in node list do
            Compute t_kj using eqn. (34) and subsequently f_kj and
            −f_kj using eqn. (35) by looping through the nodes k
            in H_j
        end
        for Node j in node list do
            Compute acceleration, velocity and displacement
            using an adaptive dynamic relaxation algorithm (Kilic
            and Madenci 2010)
        end
    end
end
```

B Additional numerical results

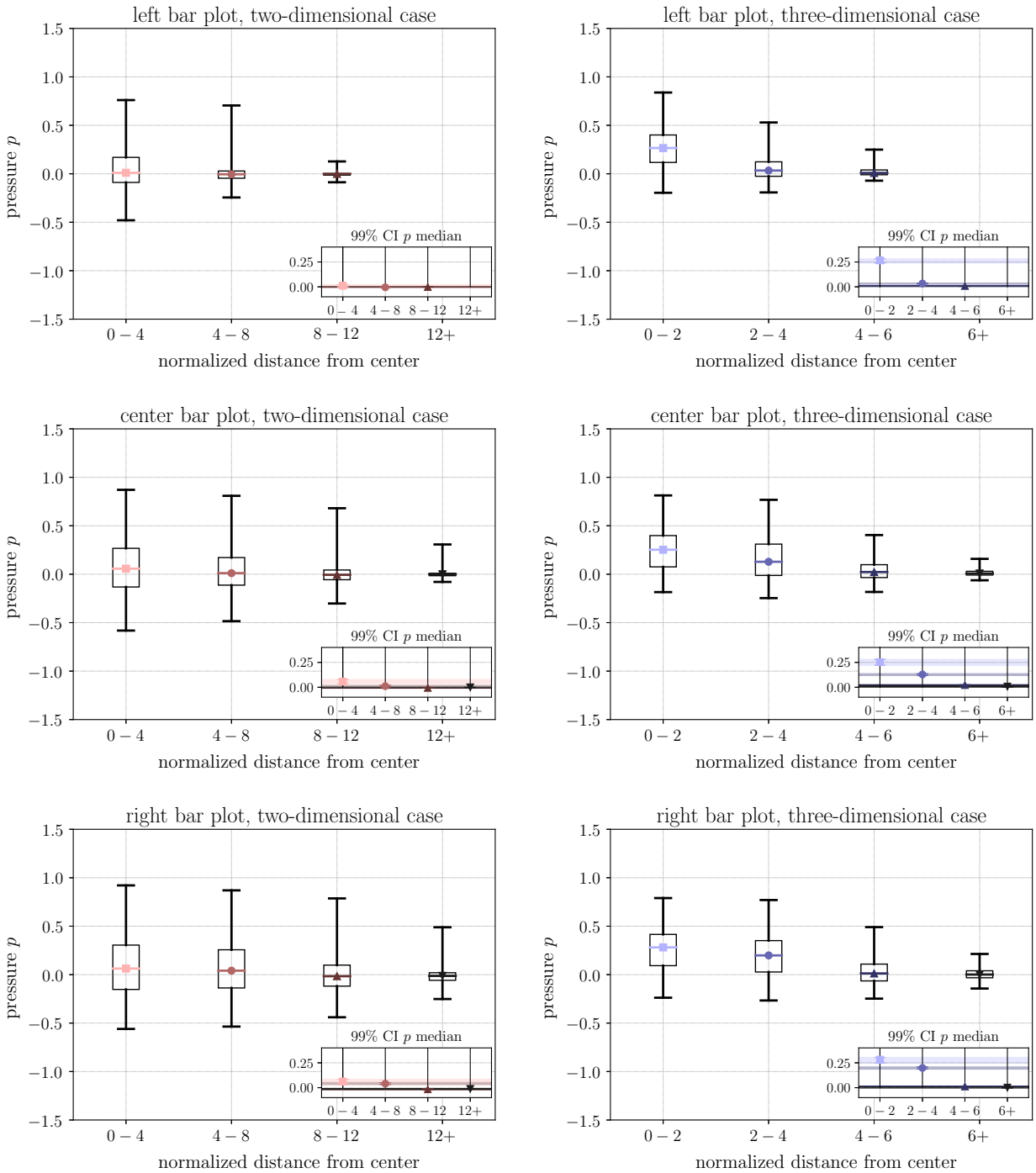

Fig. 9 Follow-up on Fig. 8, plots correspond to data presented in "left bar plot", "right bar plot", and "center bar plot". Spatial distribution of p (kPa) at different points of the simulation for 200 two-dimensional and 200 three-dimensional stochastic simulations. Growth is unsynchronized and suppressed when the cell experiences isochoric stress p above a certain threshold following Eq. (11), and cell division orientation is determined by the long axis rule following Eqs. (17) and (18). In the box plots, the box covers 50% of the data while the whiskers cover 95%. The inset plots show the bootstrap confidence interval around the medians of each distance group. From these plots, it is clear that the values of p are highly variable. In the three-dimensional case, p tends to increase significantly toward the population center, indicating compression. This behavior is consistent throughout the simulation and seen in all three stages of the simulation plotted here

References

Akanuma T, Chen C, Sato T, Merks R, Sato T (2016) Memory of cell shape biases stochastic fate decision-making despite mitotic rounding. Nat Commun 7:11963

Ambrosi D, Mollica F (2002) On the mechanics of a growing tumor. Int J Eng Sci 40:1297–1316

Ambrosi D, Pezzuto S (2012) Active stress versus active strain in mechanobiology: constitutive issues. J Elast 107(2):199–212

Ambrosi D, Preziosi L (2008) Cell adhesion mechanisms and stress relaxation in the mechanics of tumours. Biomech Model Mechanobiol 8(5):397–413

Ambrosi D, Ateshian G, Arruda E, Cowin S, Dumais J, Goriely A, Holzapfel G, Humphrey J, Kemkemer R, Kuhl E et al (2011) Perspectives on biological growth and remodeling. J Mech Phys Solids 59(4):863–883

Ambrosi D, Preziosi L, Vitale G (2012) The interplay between stress and growth in solid tumors. Mech Res Commun 42:87–91

Ambrosi D, Pezzuto S, Riccobelli D, Stylianopoulos T, Ciarletta P (2016) Solid tumors are poroelastic solids with a chemo mechanical feedback on growth. J Elast 129:1–18

Araujo RP, McElwain DLS (2004) A linear-elastic model of anisotropic tumour growth. Eur J Appl Math 15(3):365–384

Bosveld F, Markova O, Guirao B, Martin C, Wang Z, Pierre A, Balakireva M, Gaugue I, Ainslie A, Christophorou N, Lubensky D (2016) Epithelial tricellular junctions act as interphase cell shape sensors to orient mitosis. Nature 530(7591):495

Breslin S, O'Driscoll L (2013) Three-dimensional cell culture: the missing link in drug discovery. Drug Discov Today 18(5):240–249

Byrne H, Drasdo D (2008) Individual-based and continuum models of growing cell populations: a comparison. J Math Biol 58(4):657–687

Byrne H, Preziosi L (2003) Modelling solid tumour growth using the theory of mixtures. Math Med Biol 20(4):341–366

Cheng G, Tse J, Jain RK, Munn L (2009) Micro-environmental mechanical stress controls tumor spheroid size and morphology by suppressing proliferation and inducing apoptosis in cancer cells. PLoS ONE 4(2):e4632

Deisboeck TS, Wang Z, Macklin P, Cristini V (2011) Multiscale cancer modeling. Annu Rev Biomed Eng 13:127–55

Dortdivanlioglu B, Javili A, Linder C (2017) Computational aspects of morphological instabilities using isogeometric analysis. Comput Methods Appl Mech Eng 316:261–279

Drasdo D, Höhme S (2005) A single-cell-based model of tumor growth in vitro: monolayers and spheroids. Phys Biol 2(3):133–147

Drasdo D, Loeffler M (2001) Individual-based models to growth and folding in one-layered tissues: intestinal crypts and early development. Nonlinear Anal Theory Methods Appl 47(1):245–256

Drasdo D, Höhme S, Block M (2007) On the role of physics in the growth and pattern formation of multi-cellular systems: what can we learn from individual-cell based models? J Stat Phys 128(1–2):287–345

Folkman J, Hochberg M (1973) Self-regulation of growth in three dimensions. J Exp Med 138(4):745–753

Galle J, Aus G, Schaller G, Beyer T, Drasdo D (2006) Individual cell based models of the spatial temporal organization of multicellular systems-achievements and limitations. Cytometry A 69(7):704–710

Galle J, Preziosi L, Tosin A (2009) Contact inhibition of growth described using a multiphase model and an individual cell based model. Appl Math Lett 22(10):1483–90

Gibson W, Veldhuis J, Rubinstein B, Cartwright H, Perrimon N, Brodland G, Nagpal R, Gibson M (2011) Control of the mitotic cleavage plane by local epithelial topology. Cell 144(3):427–438

Gillies TE, Cabernard C (2011) Cell division orientation in animals. Curr Biol 21(15):R599–R609

Giverso C, Ciarletta P (2016) On the morphological stability of multicellular tumour spheroids growing in porous media. Eur Phys J E Soft Matter Biol Phys 39(10):92

Guz N, Dokukin M, Kalaparthi V, Sokolov I (2014) If cell mechanics can be described by elastic modulus: study of different models and probes used in indentation experiments. Biophys J 107(3):564–575

Helmlinger G, Netti PA, Lichtenbeld HC, Melder RJ, Jain RK (1997) Solid stress inhibits the growth of multicellular tumor spheroids. Nat Biotechnol 15:778–783

Hertwig O (1884) Investigations on the morphology and physiology of the cell: the problem of fertilization and isotropy of the egg, a theory of heredity, vol 3. Fischer

Jagiella N, Müller B, Müller M, Vignon-Clementel I, Drasdo D (2016) Inferring growth control mechanisms in growing multi-cellular spheroids of nsclc cells from spatial-temporal image data. PLoS Comput Biol 12(2):1004,412

Janet M, Cheng G, Tyrrell J, Wilcox-Adelman S, Boucher Y, Jain R, Munn L (2012) Mechanical compression drives cancer cells toward invasive phenotype. Proc Natl Acad Sci 109(3):911–916

Jones A, Byrne H, Gibson J, Dold J (2000) A mathematical model of the stress induced during avascular tumour growth. J Math Biol 40(6):473–499

Keyomarsi K, Sandoval L, Band V, Pardee A (1991) Synchronization of tumor and normal cells from g1 to multiple cell cycles by lovastatin. Cancer Res 51(13):3602–3609

Kilic B, Madenci E (2010) An adaptive dynamic relaxation method for quasi-static simulations using the peridynamic theory. Theor Appl Fract Mech 53(3):194–204

Kim Y, Stolarska MA, Othmer HG (2007) A hybrid model for tumor spheroid growth in vitro I: theoretical development and early results. Math Models Methods Appl Sci 17:1773–1798

Lai V, Nedrelow D, Lake S, Kim B, Weiss E, Tranquillo R, Barocas V (2016) Swelling of collagen-hyaluronic acid co-gels: an in vitro residual stress model. Ann Biomed Eng 44(10):2984–2993

Lamb B, Luo W, Nagdas S, Yousaf M (2014) Cell division orientation on biospecific peptide gradients. ACS Appl Mater Interfaces 6(14):11523–11528

Lejeune E, Linder C (2017a) Modeling tumor growth with peridynamics. Biomech Model Mechanobiol 1–17

Lejeune E, Linder C (2017b) Quantifying the relationship between cell division angle and morphogenesis through computational modeling. J Theor Biol 418:1–7

Lejeune E, Javili A, Weickenmeier JE, Kuhl Linder C (2016) Tri-layer wrinkling as a mechanism for anchoring center initiation in the developing cerebellum. Soft Matter 12:5613–5620

Lima E, Almeida R, Oden J (2015) Analysis and numerical solution of stochastic phase field models of tumor growth. Numer Methods Partial Differ Equ 31(2):552–574

Littlewood D (2015) Roadmap for peridynamic software implementation. SAND Report, Sandia National Laboratories, Albuquerque, NM and Livermore, CA

Lorenzo G, Scott M, Tew K, Hughes T, Zhang Y, Liu L, Vilanova G, Gomez H (2016) Tissue-scale, personalized modeling and simulation of prostate cancer growth. Proc Natl Acad Sci 113(48):E7663–E7671

Madenci E, Oterkus E (2014) Peridynamic theory and its applications. Springer, New York

Mascheroni P, Boso D, Preziosi L, Schrefler B (2017) Evaluating the influence of mechanical stress on anticancer treatments through a multiphase porous media model. J Theor Biol 421:179–188

Minc N, Piel M (2012) Predicting division plane position and orientation. Trends Cell Biol 22(4):193–200

Minc N, Burgess D, Chang F (2011) Influence of cell geometry on division-plane positioning. Cell 144(3):414–426

Mpekris F, Angeli S, Pirentis A, Stylianopoulos T (2015) Stress-mediated progression of solid tumors: effect of mechanical stress on tissue oxygenation, cancer cell proliferation, and drug delivery. Biomech Model Mechanobiol 14(6):1391–1402

Nestor-Bergmann A, Goddard G, Woolner S (2014) Force and the spindle: mechanical cues in mitotic spindle orientation. Semin Cell Dev Biol 34:133–139

Oterkus S (2015) Peridynamics for the solution of multiphysics problems. PhD thesis, The University of Arizona

Preziosi L, Tosin A (2008) Multiphase modelling of tumour growth and extracellular matrix interaction: mathematical tools and applications. J Math Biol 58(4):625–656

Price A, Huang E, Sebastiano V, Dunn A (2017) A semi-interpenetrating network of polyacrylamide and recombinant basement membrane allows pluripotent cell culture in a soft, ligand-rich microenvironment. Biomaterials 121:179–192

Rahman M, Feng Y, Yankeelov T, Oden J (2017) A fully coupled space-time multiscale modeling framework for predicting tumor growth. Comput Methods Appl Mech Eng 320:261–286

Ren H, Zhuang X, Cai Y, Rabczuk T (2016) Dual-horizon peridynamics. Int J Numer Meth Eng 108(12):1451–1476

Roose T, Netti P, Munn L, Boucher Y, Jain R (2003) Solid stress generated by spheroid growth estimated using a linear poroelasticity model. Microvasc Res 66(3):204–212

Silling S, Askari E (2005) A meshfree method based on the peridynamic model of solid mechanics. Comput Struct 83(17):1526–1535

Silling SA (2000) Reformulation of elasticity theory for discontinuities and long-range forces. J Mech Phys Solids 48:175–209

Silling SA, Lehoucq RB (2010) Peridynamic theory of solid mechanics. Adv Appl Mech 44:73–168

Silling SA, Epton M, Weckner O, Xu J, Askari E (2007) Peridynamic states and constitutive modeling. J Elast 88(2):151–184

Stylianopoulos T (2017) The solid mechanics of cancer and strategies for improved therapy. J Biomech Eng 139(2):021,004

Stylianopoulos T, Martin J, Chauhan V, Jain S, Diop-Frimpong B, Bardeesy N, Smith B, Ferrone C, Hornicek F, Boucher Y, Munn L (2012) Causes, consequences, and remedies for growth-induced solid stress in murine and human tumors. Proc Natl Acad Sci 109(38):15101–15108.

Stylianopoulos T, Martin J, Snuderl M, Mpekris F, Jain S, Jain R (2013) Coevolution of solid stress and interstitial fluid pressure in tumors during progression: implications for vascular collapse. Cancer Res 73(13):3833–3841

Su Y, Chiang P, Cheng L, Lee C, Swami N, Chou C (2015) High aspect ratio nanoimprinted grooves of poly (lactic-co-glycolic acid) control the length and direction of retraction fibers during fibroblast cell division. Biointerphases 10(4):041,008

Sugimura K, Lenne P, Graner F (2016) Measuring forces and stresses in situ in living tissues. Development 143(2):186–196

Sutherland RM (1988) Cell and environment interactions in tumor microregions: the multicell spheroid model. Science 240(4849):177–184

Taber L (1995) Biomechanics of growth, remodeling, and morphogenesis. Appl Mech Rev 48(8):487–545

Tepole AB, Kuhl E (2016) Computational modeling of chemo-biomechanical coupling: a systems-biology approach toward wound healing. Comput Methods Biomech Biomed Eng 19(1):13–30

Théry M, Jiménez-Dalmaroni A, Racine V, Bornens M, Jülicher F (2007) Experimental and theoretical study of mitotic spindle orientation. Nature 447(7143):493–496

Vavourakis V, Wijeratne P, Shipley R, Loizidou M, Stylianopoulos T, Hawkes D (2017) A validated multiscale in-silico model for mechano-sensitive tumour angiogenesis and growth. PLoS Comput Biol 13(1):e1005,259

Voutouri C, Polydorou C, Papageorgis P, Gkretsi V, Stylianopoulos T (2016) Hyaluronan-derived swelling of solid tumors, the contribution of collagen and cancer cells, and implications for cancer therapy. Neoplasia 18(12):732–741

Wang Z, Butner J, Kerketta R, Cristini V, Deisboeck TS (2015) Simulating cancer growth with multiscale agent-based modeling. Semin Cancer Biol 30:70–78

Wyatt T, Harris A, Lam M, Cheng Q, Bellis J, Dimitracopoulos A, Kabla A, Charras G, Baum B (2015) Emergence of homeostatic epithelial packing and stress dissipation through divisions oriented along the long cell axis. Proc Natl Acad Sci 112(18):5726–5731

Xue S, Li B, Feng X, Gao H (2016) Biochemomechanical poroelastic theory of avascular tumor growth. J Mech Phys Solids 94:409–432